

# DualSeg: Unified Multi-Scale Framework With Dual-Stage Encoder For Glomerular Segmentation

Yan Zhang<sup>ID</sup>, Wei Yuan<sup>ID</sup>, Jiayu Zhang<sup>ID</sup>, Jing Zhang<sup>ID</sup>, Ling He<sup>ID</sup>

**Abstract**—Chronic Kidney Disease (CKD) requires accurate histopathological analysis of glomeruli, but manual segmentation in Whole Slide Images (WSIs) is labor-intensive and error-prone. Existing methods such as Convolutional Neural Networks (CNNs) suffer from limited adaptability to global context, while Vision Transformers (ViTs) incur high computational costs, failing to simultaneously address local texture discriminability, spatial heterogeneity, and multi-scale morphological prior mapping in glomerular segmentation. To tackle these challenges, we propose DualSeg, a unified dual-stage hybrid framework integrating CNN and Vision Recurrent Weighted Key Value (VRWKV). The framework employs a two-stage encoder: Wave-Swin Blocks with dynamic propagation windows for multi-directional local feature extraction, and VRWKV Blocks with a Z-Shift operator to model long-range dependencies efficiently via linear attention while preserving edge integrity. A lightweight decoder with Non-negative Matrix Factorization (NMF) further enhances multi-scale feature fusion. Evaluated on three datasets (murine KPIs, human HuBMAP, and human KPMP), DualSeg outperforms state-of-the-art (SOTA) models, achieving superior average mDSC (92.98% on KPIs, 89.79% private mDSC on HuBMAP, 81.95% on KPMP) and the lowest HD95. It also demonstrates robust cross-species and cross-center generalizability through direct inference on human datasets without retraining. DualSeg bridges local texture sensitivity and global context modeling, providing a new methodological approach for renal histology analysis. The model code is available in <https://github.com/unsky/DualSeg>.

**Index Terms**—Chronic Kidney Disease (CKD), Histopathology Image Analysis, Glomerular Segmentation, Convolutional Neural Network (CNN), Vision Recurrent Weighted Key Value(VRWKV)

## I. INTRODUCTION

Chronic Kidney Disease (CKD) affects over 9% of the global population, leading to systemic complications such as hypertension [1]–[3]. Its primary histological manifestations include glomerulosclerosis and renal interstitial fibrosis [4], [5], making pathological alterations in the glomerulus a focal point for therapeutic interventions. However, expert manual analysis of Whole Slide Images (WSIs) is labor-intensive and

resource-demanding [6]. Consequently, advanced computational tools for automated, high-precision glomerulus segmentation are essential to overcome these diagnostic bottlenecks.

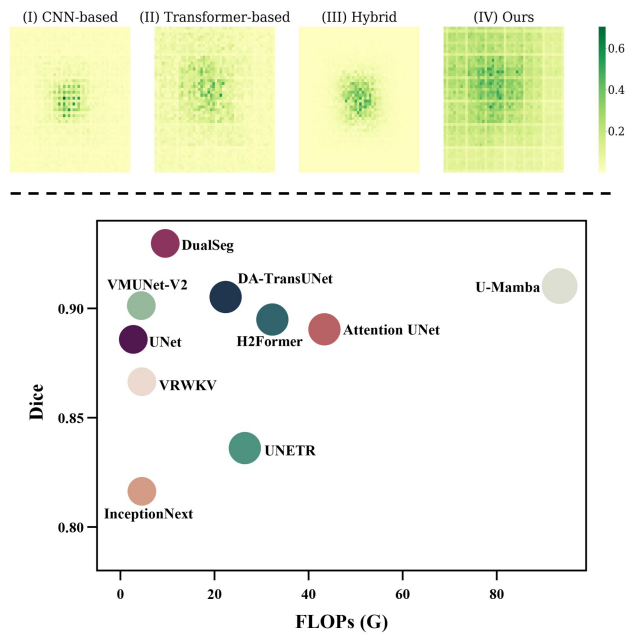


Fig. 1: **Top:** Visualization of the *Effective Receptive Fields* (ERF) for different architectures. CNNs (I) focus locally, while Transformers (II) capture global but noisy patterns. Our method (IV) achieves a clean, global ERF. **Bottom:** Performance vs. FLOPs comparison. DualSeg (top-left) achieves the optimal trade-off between segmentation accuracy and computational efficiency.

Accurate glomerular segmentation remains challenging due to the complex interplay between local texture and global structure. Three core technical hurdles define this task: (1) *Local texture discriminability*: Glomeruli exhibit diverse substructures and high intra-class variability [12], [13]. (2) *Spatial heterogeneity*: The irregular distribution of glomeruli necessitates global contextual information for structural continuity [14]. (3) *Multi-scale mapping of morphological priors*: Effective perception requires integrating receptive fields at varying resolutions to decode both fine-grained details and macroscopic priors [14]–[16]. Addressing these challenges

Corresponding author: Ling He

Yan Zhang, Wei Yuan, Jiayu Zhang, Jing Zhang and Ling He are with the College of Biomedical Engineering, Sichuan University, Chengdu 610065, China (e-mail: zzzzy@stu.scu.edu.cn; yuanw@stu.scu.edu.cn; zhang.jiayu@stu.scu.edu.cn; jing.zhang@scu.edu.cn; ling.he@scu.edu.cn).

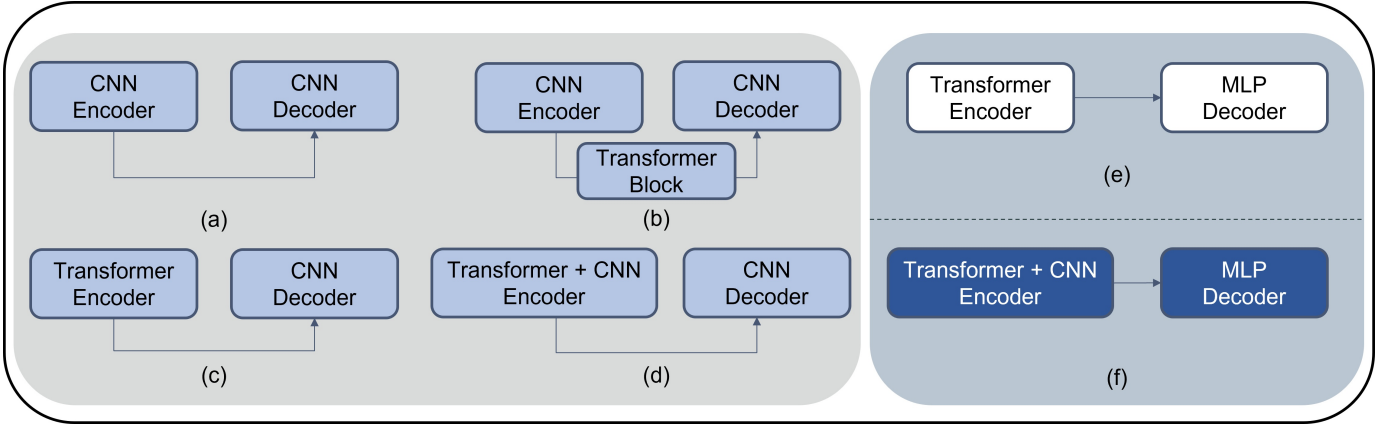


Fig. 2: Comparison of segmentation architectures. (a–d) represent **U-shaped** designs: (a) Pure CNN (UNet [7]); (b–d) Hybrid Cascades (TransUNet [8], UNETR [9] and H2Former [10]). (e–f) represent **Pyramid-shaped** designs: (e) Pure Transformer (SegFormer [11]); (f) Our **DualSeg**, a hierarchical hybrid encoder with multi-scale fusion.

requires a unified architecture balancing pixel-level precision with global context.

Deep learning has revolutionized digital pathology. Convolutional Neural Networks (CNNs) address the first challenge (local texture) via inductive biases and parameter sharing [8], [17]. For example, Kaur et al. [18] demonstrated UNet’s efficacy in modeling sub-pixel intensity transitions in PAS-stained boundaries. However, CNNs inherently struggle with long-range dependencies due to their limited Effective Receptive Field (ERF) [8], [10], [19], as visualized in Fig. 1(I), constraining their ability to resolve complex morphologies.

Conversely, Vision Transformers (ViTs) address the second challenge (spatial heterogeneity) by leveraging self-attention for global context [20], [21], as shown in Fig. 1(II). ViTs typically outperform UNets in maintaining structural continuity amidst fibrosis-induced fragmentation [21]. Yet, the quadratic complexity of self-attention limits their utility in high-resolution histology [10]. To mitigate this, efficient alternatives like Wave-MLP [22] (preserving structure via spatial-wise convolutions) and VRWKV [23] (linear-time recurrent kernels) have emerged. Similarly, VM-UNet [24] introduced State Space Models (SSM) to harmonize efficiency and performance.

Beyond standalone architectures, synergistic hybrid frameworks have been explored. As illustrated in Fig. 2(a-d), most prior hybrids (e.g., TransUNet [8], H2Former [10] and U-mamba [25]) adopt U-shaped paradigms. However, these often suffer from limitations: TransUNet compromises multi-scale capture; H2Former’s shallow integration underutilizes ViTs; and their ERFs often remain suboptimal (Fig. 1(III)). Distinct from U-shaped models, pyramid architectures like SegFormer [11] (Fig. 2(e)) and SegNext [26] address the third challenge via feature fusion but rely on unidirectional extraction, weakening robustness against morphological variations. This prompts a critical inquiry: *Is it possible to integrate local and global features within a unified multi-scale framework to tackle all three segmentation challenges simultaneously?*

To answer this, we propose **DualSeg**, a novel hybrid framework synergizing Wave Vision and VRWKV within a

pyramid structure (Fig. 2(f)). Specifically, our architecture employs a dual-stage encoder: early-stage Wave-Swin blocks perform hierarchical local feature extraction to resolve texture discriminability, while later-stage VRWKV blocks model long-range dependencies via linear attention to address spatial heterogeneity. This design combines the texture sensitivity of CNNs, the generalization of MLPs, and the scalability of VRWKV. By bridging local and global processing, DualSeg achieves robust multi-scale mapping of morphological priors. As demonstrated in Fig. 1, our model achieves a global, clean ERF (IV) and delivers SOTA performance with optimal computational efficiency (Bottom).

The main contributions of this study are:

- We propose **DualSeg**, a novel pyramid hybrid architecture integrating convolutional local extraction with linear-complexity bidirectional attention to address texture, heterogeneity, and multi-scale challenges.
- We design a plug-and-play attention module based on wave vision to capture multi-directional semantic features, enhancing representation learning.
- We validate robust cross-species and cross-center generalizability by training on mouse data and performing direct inference on a held-out human dataset, demonstrating clinical viability.
- Our method achieves SOTA performance across three 2D glomerulus segmentation datasets, outperforming existing approaches in both accuracy and robustness.

## II. RELATED WORK

### A. Development of Medical Image Analysis and Kidney Pathology Image Segmentation

Deep learning has fundamentally transformed medical image analysis, particularly within the domain of pathological image segmentation [27], [28]. This paradigm shift has enabled end-to-end hierarchical feature learning from WSIs, delivering enhanced accuracy and robustness in segmenting diverse organs and lesions while effectively overcoming challenges associated with morphological heterogeneity and subtle pathological variations [29].

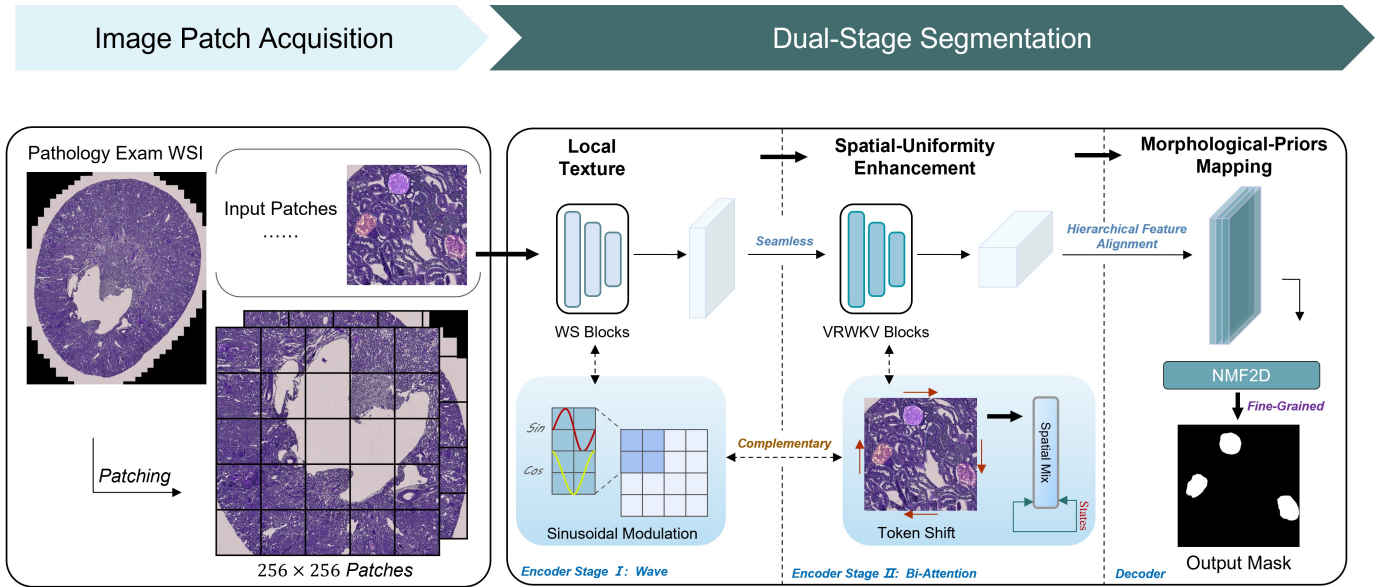


Fig. 3: Overview of the proposed **DualSeg**. The original image is fed into the Dual-Stage encoder composed of Wave-Swin Block and VRWKV Block to extract local texture and patial heterogeneity. Next, the features are merged and refined by the lightweight *Hamburger* decoder to obtain the predicted glomerular mask. The composition of main modules is explained in detail.

In renal pathology, automated glomerular segmentation has become a pivotal diagnostic tool, given the glomerulus's status as the kidney's core functional unit [30]. Early methodologies relied on combining manual annotations with traditional machine learning for boundary detection [31], [32], utilizing handcrafted morphometric and textural features. However, these approaches suffered from limited generalizability and high susceptibility to staining inconsistencies and annotation biases [33]. The advent of deep learning, particularly Convolutional Neural Networks (CNNs), marked a significant leap forward. CNNs demonstrated superior capability over Recurrent Neural Networks (RNNs) and Artificial Neural Networks (ANNs) in decoding intricate glomerular morphologies from high-resolution WSIs [34]–[38]. Landmark studies have validated this progress: Marsh et al. [39] achieved pathologist-level accuracy in discriminating sclerotic glomeruli, while Bueno et al. [40] pioneered pixel-wise semantic segmentation for glomerulosclerosis detection. These innovations have not only refined diagnostic precision for diseases like diabetic nephropathy but also established a foundation for quantitative, standardized renal function assessment.

Addressing data scarcity, Andreini et al. [41] demonstrated that pre-training on murine models followed by fine-tuning on human datasets significantly enhances generalization in human glomerular segmentation. This finding highlights the clinical utility of cross-species transfer learning as a viable paradigm to bridge preclinical research and clinical application, particularly when annotated human pathological data is restricted.

#### B. Technological Evolution of Glomerular Segmentation Architectures

The evolution of semantic segmentation architectures has driven continuous performance gains in glomerular analy-

sis. CNNs established the foundational framework, with U-Net based innovations—such as the DeepLab series (notably DeepLabv3+ utilizing atrous convolution)—proving effective in handling glomerular morphological variability [15], [42]. These studies underscore that U-Net variants, leveraging encoder-decoder structures with skip connections, effectively fuse high-level semantics with low-level spatial details, a capability critical for distinguishing glomeruli from adjacent tubules and interstitium [15].

However, the computational efficiency of pure convolution models has been scrutinized. To address this, lightweight architectures like UNet and MLP-UNet introduced Multi-Layer Perceptrons (MLPs) to optimize the trade-off between inference speed and parameter count, thereby improving generalizability while reducing computational burden [43]–[45]. Notably, these models achieved competitive performance with approximately 70% fewer parameters than traditional U-Net variants.

More recently, frameworks based on self-attention mechanisms, such as SegFormer and U-Mamba, have pioneered a new paradigm. By capturing long-range spatial correlations, these models outperform CNN-based methods in delineating irregularly shaped glomeruli [11], [23], [25], [28], [46]–[48]. Inspired by this success, hybrid architectures integrating local convolutional extraction with global transformer-based modeling have pushed performance boundaries further, achieving superior results on benchmarks like the HuBMAP dataset [13].

Despite these advances, existing frameworks continue to struggle with precise boundary delineation in complex scenarios, such as distinguishing sclerotic capsules from surrounding fibrosis, and lack robust generalizability across diverse pathological conditions. While studies such as [53], [54] and [21] have attempted to mitigate these issues through ensemble

**TABLE I: PERFORMANCE COMPARISON FOR GLOMERULAR SEGMENTATION ON THE FIVE-FOLD CROSS-VALIDATION OF THE KPIs DATASET WITH RESPECT TO EXISTING METHODS**

Models	DN			NEP25			Normal			5/6Nx			AVG		
	mDSC↑	HD95↓	IoU↑	mDSC↑	HD95↓	IoU↑	mDSC↑	HD95↓	IoU↑	mDSC↑	HD95↓	IoU↑	mDSC↑	HD95↓	IoU↑
U-Net [7]	0.8973 ±0.0025	74.9936 ±2.3086	0.8737 ±0.0027	0.8737 ±0.0028	76.5603 ±1.8606	0.8469 ±0.0029	0.9091 ±0.0023	77.0467 ±2.4556	0.8860 ±0.0025	0.8332 ±0.0032	160.2147 ±2.7958	0.8052 ±0.0034	0.8859 ±0.2657	93.3440 ±2.4627	0.8628 ±0.0028
Attention U-Net [49]	0.9006 ±0.0025	60.0169 ±1.9383	0.8784 ±0.0026	0.8837 ±0.0027	85.9233 ±2.1759	0.8588 ±0.0028	0.9153 ±0.0023	69.4993 ±2.2980	0.8940 ±0.0024	0.8237 ±0.0033	204.4328 ±3.4987	0.7976 ±0.0035	0.8905 ±0.0026	97.0253 ±2.5783	0.8676 ±0.0028
SegNext [26]	0.9242 ±0.0022	77.6273 ±2.4398	0.9066 ±0.0023	0.9168 ±0.0023	256.4412 ±2.3992	0.8984 ±0.0024	0.9331 ±0.0021	68.0672 ±2.2544	0.9157 ±0.0022	0.8444 ±0.0032	253.6379 ±0.0032	0.8236 ±0.0033	0.9118 ±0.0024	109.2467 ±0.0024	0.8935 ±0.0025
DeepLabv3+ [42]	0.9283 ±0.0022	77.1417 ±2.4108	0.9115 ±0.0023	0.9213 ±0.0023	80.2639 ±2.0792	0.9044 ±0.0024	0.9356 ±0.0020	64.7229 ±2.2177	0.9188 ±0.0021	0.8466 ±0.0032	240.0954 ±3.9110	0.8254 ±0.0033	0.9147 ±0.0024	103.9777 ±2.7477	0.8970 ±0.0025
Wave-MLP [22]	0.9299 ±0.0021	71.4539 ±2.4084	0.9133 ±0.0022	0.9189 ±0.0023	77.6752 ±2.0753	0.9006 ±0.0024	0.9361 ±0.0020	62.6423 ±2.1879	0.9189 ±0.0021	0.8375 ±0.0033	274.2791 ±4.1231	0.8153 ±0.0034	0.9131 ±0.0024	108.5067 ±2.8366	0.8949 ±0.0025
InceptionNext [50]	0.7798 ±0.0037	279.4065 ±3.5819	0.7510 ±0.0038	0.8445 ±0.0030	117.9740 ±2.3975	0.8136 ±0.0032	0.8490 ±0.0030	113.4765 ±2.3526	0.8165 ±0.0031	0.7333 ±0.0041	375.5270 ±4.5353	0.7116 ±0.0042	0.8164 ±0.0033	187.3932 ±3.2660	0.7869 ±0.0035
SegFormer [11]	0.9332 ±0.0021	71.8198 ±2.3607	0.9174 ±0.0022	0.9235 ±0.0023	85.5397 ±2.2958	<b>0.9064</b> <b>±0.0023</b>	0.9363 ±0.0020	65.9465 ±2.2332	0.9194 ±0.0021	0.8166 ±0.0035	325.5992 ±4.5238	0.7964 ±0.0036	0.9102 ±0.0025	121.5121 ±3.0465	0.8927 ±0.0026
VRWKV [23]	0.9330 ±0.0021	70.7004 ±2.3996	0.9176 ±0.0022	0.9232 ±0.0023	77.5173 ±2.1069	0.9061 ±0.0024	<b>0.9370</b> <b>±0.0020</b>	61.6787 ±2.1709	<b>0.9201</b> <b>±0.0021</b>	0.8738 ±0.0029	188.1708 ±3.4140	0.8518 ±0.0030	0.9013 ±0.0028	90.5756 ±2.5482	0.8942 ±0.0027
VM-UNET-V2 [48]	0.8983 ±0.0025	95.4675 ±2.5092	0.8757 ±0.0027	0.8843 ±0.0027	113.2830 ±2.4918	0.8604 ±0.0028	0.9077 ±0.0024	87.9016 ±2.4350	0.8850 ±0.0025	0.7248 ±0.0042	390.3619 ±5.1129	0.7099 ±0.0043	0.8665 ±0.0030	153.0778 ±3.3923	0.8452 ±0.0031
UNETR [9]	0.8667 ±0.0028	93.1881 ±2.3828	0.8382 ±0.0030	0.8187 ±0.0033	146.9859 ±2.5678	0.7874 ±0.0034	0.8745 ±0.0027	79.2260 ±2.1871	0.8450 ±0.0029	0.7243 ±0.0042	394.2254 ±4.8802	0.7059 ±0.0043	0.8361 ±0.0032	153.2457 ±3.2384	0.8088 ±0.0033
Swin UNETR [51]	0.9142 ±0.0023	85.0643 ±2.5062	0.8945 ±0.0025	0.9025 ±0.0025	86.2819 ±2.0911	0.8810 ±0.0026	0.9158 ±0.0024	78.0189 ±2.4094	0.9067 ±0.0023	0.7223 ±0.0043	462.2809 ±5.5391	0.7081 ±0.0043	0.8801 ±0.0029	157.4215 ±3.6115	0.8615 ±0.0030
DA-TransUNet [52]	0.9190 ±0.0023	88.3991 ±2.4660	0.9004 ±0.0024	0.9111 ±0.0024	80.9081 ±2.0693	0.8917 ±0.0025	0.9278 ±0.0021	82.5779 ±2.5860	0.9095 ±0.0022	0.7823 ±0.0038	334.6921 ±4.4253	0.7619 ±0.0039	0.8950 ±0.0027	134.0005 ±3.1449	0.8761 ±0.0028
H2Former [10]	0.9259 ±0.0022	73.2565 ±2.3295	0.9082 ±0.0023	0.9173 ±0.0023	80.9923 ±1.9999	0.8993 ±0.0024	0.9315 ±0.0021	65.9763 ±2.2418	0.9135 ±0.0022	0.8141 ±0.0035	307.6074 ±4.4570	0.7936 ±0.0036	0.9052 ±0.0025	117.6038 ±2.9761	0.8868 ±0.0026
U-mamba [25]	0.8794 ±0.0027	75.3772 ±1.8672	0.8545 ±0.0029	0.8799 ±0.0028	82.9104 ±1.8076	0.8563 ±0.0029	0.9172 ±0.0023	63.2446 ±2.1390	0.8980 ±0.0024	0.7355 ±0.0041	325.2652 ±4.2271	0.7151 ±0.0042	0.8693 ±0.0027	120.3657 ±2.8212	0.8487 ±0.0031
DualSeg(ours)	<b>0.9603</b> <b>±0.0012</b>	<b>62.9389</b> <b>±1.7681</b>	<b>0.9386</b> <b>±0.0014</b>	<b>0.9349</b> <b>±0.0016</b>	<b>74.7815</b> <b>±1.5739</b>	0.9055 ±0.0018	0.9187 ±0.0005	<b>33.2828</b> <b>±1.1220</b>	0.8537 ±0.0008	<b>0.9007</b> <b>±0.0022</b>	<b>149.6097</b> <b>±2.5757</b>	<b>0.8677</b> <b>±0.0025</b>	<b>0.9298</b> <b>±0.0016</b>	<b>66.8485</b> <b>±1.7330</b>	<b>0.8967</b> <b>±0.0019</b>

modeling, this approach inevitably incurs high computational overhead, limiting its feasibility for real-time clinical analysis.

### III. METHODOLOGY

In this section, we present a comprehensive overview of our proposed architecture, DualSeg, designed for the precise extraction and synthesis of multi-scale textural features from glomeruli in renal histopathological images. The architecture, illustrated in Fig. 3, is composed of three core components: (1) a dual-stage hybrid encoder that integrates an initial-stage Wave-Attention Block for local feature refinement, (2) a subsequent-stage VRWKV module for global context modeling, and (3) a lightweight decoder for efficient feature aggregation. This modular design ensures robust representation learning while maintaining computational efficiency, addressing the dual challenges of fine-grained texture discrimination and long-range dependency modeling in complex pathological scenarios.

#### A. Wave-Swin Block

To address the dual challenges of fine-grained texture discrimination and global contextual modeling in renal glomerular segmentation, we propose a hybrid Dual-Stage encoder that seamlessly integrates an improved CNN-based first stage with a VRWKV-based second stage. Specifically, the initial stage employs our proposed Wave-Swin (WS) Block to capture local glomerular boundaries. By introducing a dynamic wave-based representation shown in Fig. 4, the WS block overcomes the static receptive field limitations of traditional wave methods, enhancing local texture discriminability. Subsequently, the

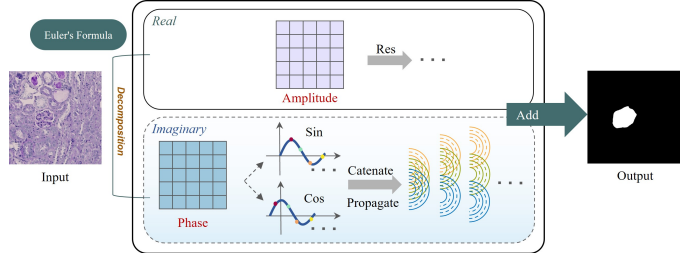


Fig. 4: Illustration of the Token-Mixing mechanism within the **Wave-Swin** Block. The input is initially decomposed into a *real* component and an *imaginary* component via Euler's formula. The modulated phase undergoes two distinct cosine transformations and window-based propagation, and is subsequently fused with the amplitude information to generate the output.

VRWKV module is utilized to model long-range dependencies, effectively handling the global irregular spatial arrangements characteristic of renal tubulointerstitial fibrosis. This synergistic design robustly bridges the gap between texture fidelity and contextual awareness in complex histopathological scenarios.

1) *Wave Formulation*: Let the input feature map be denoted as  $\mathbf{X} = [\mathbf{x}_1, \mathbf{x}_2, \dots, \mathbf{x}_n]$ , where each  $\mathbf{x}_j$  represents a token. Instead of standard linear projections, we map these tokens into a complex wave representation to capture both semantic intensity and spatial structural priors.

We define the complex wave form  $\mathbf{z}_j$  for the  $j$ -th token as:

$$\mathbf{z}_j = \mathcal{A}(\mathbf{x}_j) \odot \exp(i \cdot \mathcal{P}(\mathbf{x}_j)), \quad (1)$$

where  $\mathcal{A}(\cdot)$  and  $\mathcal{P}(\cdot)$  denote learnable linear transformations

TABLE II: PERFORMANCE COMPARISON FOR GLOMERULAR SEGMENTATION ON THE TEST SET OF THE HUBMAP DATASET WITH RESPECT TO EXISTING METHODS

Models	mDSC↑											
	Fold1		Fold2		Fold3		Fold4		Fold5		AVG	
	Private	Public	Private	Public								
UNet [7]	0.8731	0.7923	0.8629	0.7812	0.8714	0.7899	0.8512	0.7865	0.8711	0.7918	$0.8659 \pm 0.0082$	$0.7883 \pm 0.0041$
Attention-UNet [49]	0.8699	0.7731	0.8661	0.7662	0.8550	0.7770	0.8408	0.7821	0.8551	0.7742	$0.8574 \pm 0.0102$	$0.7745 \pm 0.0052$
SegNext [26]	0.7834	0.7447	0.7608	0.7244	0.7597	0.7445	0.6938	0.7108	0.7416	0.7117	$0.7479 \pm 0.0301$	$0.7272 \pm 0.0150$
DeepLabV3+ [42]	0.8658	0.7901	0.8750	0.7742	0.8726	0.7821	0.8307	0.7805	0.8307	0.7805	$0.8550 \pm 0.0200$	$0.7815 \pm 0.0051$
Wave-MLP [22]	0.8753	0.7996	0.8461	0.7843	0.8669	0.8063	0.8474	0.8002	0.8684	0.7701	$0.8608 \pm 0.0118$	$0.7921 \pm 0.0132$
InceptionNext [50]	0.7902	0.7233	0.7698	0.7532	0.7909	0.7341	0.7102	0.6810	0.7606	0.7225	$0.7943 \pm 0.0295$	$0.7228 \pm 0.0237$
SegFormer [11]	0.8926	0.8120	0.8795	0.7832	0.8855	0.8048	0.8908	0.8098	0.8781	0.8158	$0.8853 \pm 0.0058$	$0.8051 \pm 0.0115$
VRWKV [23]	0.8931	0.8330	0.8814	0.8171	0.8877	0.8006	0.8680	0.7901	0.8886	0.8263	$0.8838 \pm 0.0087$	$0.8134 \pm 0.0159$
VM-UNET-V2 [48]	0.8772	0.7913	0.8488	0.7818	0.8555	0.7917	0.8322	0.7996	0.8661	0.7400	$0.8560 \pm 0.0153$	$0.7809 \pm 0.0212$
UNETR [9]	0.5819	0.5725	0.6329	0.6267	0.5819	0.5916	0.5728	0.5757	0.6457	0.6171	$0.6030 \pm 0.0301$	$0.5967 \pm 0.0218$
Swin-UNETR [51]	0.8559	0.7718	0.8531	0.7546	0.8552	0.7768	0.8571	0.7764	0.8313	0.7666	$0.8505 \pm 0.0097$	$0.7692 \pm 0.0082$
DA-TransUNet [52]	<b>0.8960</b>	0.7911	0.8944	0.7692	<b>0.9019</b>	0.7906	0.8887	0.7931	0.8866	0.7864	$0.8935 \pm 0.0054$	$0.7861 \pm 0.0087$
H2Former [10]	0.7991	0.7075	0.7644	0.6808	0.8151	0.7547	0.6443	0.5675	0.7825	0.7298	$0.7611 \pm 0.0608$	$0.6881 \pm 0.0650$
U-mamba [25]	0.8667	0.7699	0.8671	0.7595	0.8543	0.7580	0.8312	0.7723	0.8600	0.7701	$0.8559 \pm 0.0132$	$0.7660 \pm 0.0060$
DualSeg(Ours)	0.8925	<b>0.8366</b>	<b>0.8948</b>	<b>0.8488</b>	0.9016	<b>0.8441</b>	<b>0.8972</b>	<b>0.8217</b>	<b>0.9032</b>	<b>0.8354</b>	<b>0.8979 ± 0.0040</b>	<b>0.8373 ± 0.0092</b>

that project the input to amplitude and phase terms, respectively. The operator  $\odot$  represents element-wise multiplication. Conceptually, the amplitude  $\mathcal{A}(\mathbf{x}_j) \in \mathbb{R}^+$  encodes the semantic intensity (e.g., texture presence), while the phase  $\mathcal{P}(\mathbf{x}_j) \in [0, 2\pi]$  encodes the token’s relative spatial position within the glomerular structure.

The phase term is strategically designed to capture zonal microanatomical variations. Specifically, glomeruli in cortical regions exhibit more compact clustering compared to those in the medulla, where fibrotic remodeling disrupts continuity. By assigning distinctive angular values based on proximity to anatomical landmarks (e.g., the renal capsule), the phase effectively models these spatial relationships.

Utilizing Euler’s formula, the complex wave  $\mathbf{z}_j$  is implicitly decomposed into orthogonal real and imaginary components. These components are then aggregated via a dynamic token-mixing operation:

$$\mathbf{y}_j = \sum_{k \in \Omega_j} (\text{Re}(\mathbf{z}_k) \mathbf{W}_{Re} + \text{Im}(\mathbf{z}_k) \mathbf{W}_{Im}), \quad (2)$$

where  $\mathbf{y}_j$  is the output token,  $\Omega_j$  denotes the dynamic propagation window centered at  $j$ , and  $\mathbf{W}_{Re}, \mathbf{W}_{Im}$  are learnable weights governing the fusion of spatial components.

2) **Dynamic Swin Mechanism:** To overcome the static receptive field limitation of prior wave-propagation windows, we propose a dynamic Swin mechanism that adaptively reshapes the waveform  $\Omega_j$ . We define a candidate set of odd-sized windows  $S = \{7, 11, 15, \dots\}$ . The selection of these anchors is informed by both domain-validated baselines and dataset-specific anatomical statistics.

First, previous studies on Wave-MLP have empirically demonstrated that windows smaller than 7 lack the generality necessary to capture spatial dependencies in medical images; meanwhile, anchor sizes 7 and 11 align with kernel sizes employed in SOTA encoders like SegNeXt. Second, the average glomerular bounding box in our murine dataset measures approximately 154px [41]. After the 4 $\times$  and 8 $\times$  downsampling stages, this dimension reduces to roughly 38px

and 19px, respectively. Accordingly, selecting a maximum window of 15 (instead of 21) prevents the network from integrating extraneous background noise while ensuring full coverage of the target glomerular structure.

For each token, a mapping function  $M : S \rightarrow \{1, 2, \dots, |S|\}$  is learned to select the optimal window size from  $S$ , ensuring the faithful encoding of diverse spatial patterns. This dynamic strategy substantially improves feature extraction by comprehensively balancing glomerular positional semantics with a broader, yet precise, contextual framework.

## B. VRWKV Block

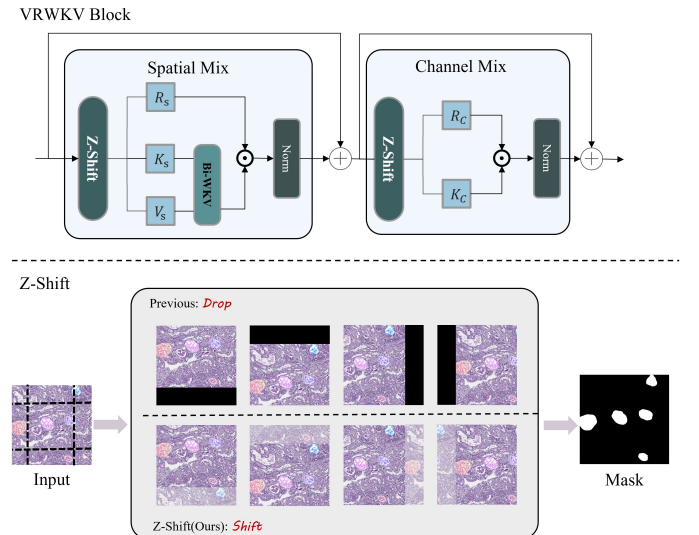


Fig. 5: Structure of the improved VRWKV block. The black margins in the lower panel illustrate the prior approach where pixels shifted beyond the boundary are simply dropped. In contrast, our **Z-Shift** wraps these pixels to the opposite edge, filling the empty regions and eliminating information loss.

Following the local feature extraction, the VRWKV block is employed to establish non-local constraints. This stage

**TABLE III: CROSS-DATASET INFERENCE PERFORMANCE COMPARISON FOR GLOMERULAR SEGMENTATION ON THE KPMP DATASET USING 5-FOLD MOUSE-TRAINED MODELS WITH RESPECT TO EXISTING METHODS**

Models	1			2			3			4			AVG		
	mDSC↑	HD95↓	IoU↑	mDSC↑	HD95↓	IoU↑	mDSC↑	HD95↓	IoU↑	mDSC↑	HD95↓	IoU↑	mDSC↑	HD95↓	IoU↑
U-Net [7]	0.3936 ±0.0045	279.4223 ±2.4890	0.5095 ±0.0045	0.2662 ±0.0042	471.9885 ±2.5648	0.2560 ±0.0042	0.5189 ±0.0047	119.5596 ±1.8510	0.4973 ±0.0047	0.5387 ±0.0046	152.3241 ±2.0956	0.5095 ±0.0045	0.4836 ±0.0046	196.2395 ±2.4062	0.4588 ±0.0046
Attention U-Net [49]	0.7165 ±0.0041	165.1443 ±2.1467	0.6875 ±0.0041	0.4762 ±0.0046	274.6819 ±2.4661	0.4540 ±0.0047	0.8431 ±0.0033	54.8253 ±1.1642	0.8230 ±0.0034	0.6953 ±0.0040	90.7108 ±1.5556	0.6559 ±0.0041	0.7056 ±0.0041	110.6999 ±1.7900	0.6736 ±0.0041
SegNext [26]	0.7926 ±0.0036	164.5795 ±2.2619	0.7656 ±0.0037	0.5235 ±0.0046	86.5286 ±2.3992	0.4978 ±0.0046	0.8488 ±0.0032	36.7357 ±0.5685	0.8277 ±0.0033	0.7287 ±0.0039	103.8195 ±1.7509	0.6948 ±0.0040	0.7410 ±0.0039	112.1102 ±1.8356	0.7116 ±0.0040
DeepLabv3+ [42]	0.7846 ±0.0038	100.0552 ±1.9003	0.7640 ±0.0038	0.6030 ±0.0043	182.8433 ±2.1006	0.5615 ±0.0043	0.8545 ±0.0031	67.7374 ±1.6939	0.8333 ±0.0032	0.6952 ±0.0041	116.7432 ±1.9572	0.6617 ±0.0041	0.7317 ±0.0040	112.6154 ±1.9438	0.7018 ±0.0040
Wave-MLP [22]	0.8152 ±0.0034	149.4421 ±2.1076	0.7899 ±0.0036	0.5158 ±0.0046	299.4355 ±2.7413	0.4929 ±0.0047	0.8505 ±0.0031	49.6731 ±0.8149	0.8253 ±0.0032	0.7675 ±0.0037	92.2304 ±1.6319	0.7342 ±0.0038	0.7646 ±0.0038	106.0041 ±1.7929	0.7353 ±0.0038
InceptionNext [50]	0.6564 ±0.0044	236.3450 ±2.3658	0.6352 ±0.0045	0.4779 ±0.0048	272.6440 ±2.6615	0.4672 ±0.0049	0.7136 ±0.0042	167.7567 ±1.9100	0.6937 ±0.0043	0.4301 ±0.0043	312.1570 ±2.4503	0.3875 ±0.0042	0.5279 ±0.0045	284.8018 ±2.4428	0.4967 ±0.0046
SegFormer [11]	0.8037 ±0.0036	125.7612 ±1.8165	0.7814 ±0.0037	<b>0.6151</b> <b>±0.0044</b>	206.3655 ±2.4028	<b>0.5815</b> <b>±0.0044</b>	0.8597 ±0.0030	47.1347 ±0.6667	0.8353 ±0.0031	0.8285 ±0.0033	<b>49.0933</b> <b>±1.1678</b>	0.7986 ±0.0033	0.8082 ±0.0035	70.7543 ±1.4692	0.7802 ±0.0035
VRWKV [23]	0.7912 ±0.0036	143.4809 ±2.1293	0.7662 ±0.0037	0.5112 ±0.0046	271.6789 ±2.2767	0.4883 ±0.0047	0.8056 ±0.0036	62.1875 ±0.1015	0.7850 ±0.0037	0.7615 ±0.0037	65.9837 ±1.3855	0.7266 ±0.0038	0.7480 ±0.0039	89.0189 ±1.6278	0.7188 ±0.0039
VM-UNET-V2 [48]	0.6521 ±0.0043	181.1196 ±1.9559	0.6233 ±0.0044	0.4833 ±0.0046	332.8376 ±2.5972	0.4575 ±0.0046	0.7880 ±0.0036	104.5297 ±0.5290	0.7620 ±0.0038	0.5410 ±0.0043	232.7710 ±2.4792	0.4963 ±0.0043	0.6028 ±0.0044	216.0202 ±2.3843	0.5664 ±0.0044
UNETR [9]	0.6199 ±0.0046	250.5465 ±2.1782	0.6050 ±0.0047	0.4500 ±0.0048	391.7400 ±2.8152	0.4416 ±0.0049	0.6436 ±0.0047	158.4295 ±1.8108	0.6349 ±0.0047	0.4899 ±0.0046	333.3864 ±2.6834	0.4416 ±0.0049	0.5369 ±0.0047	308.9828 ±2.6276	0.5193 ±0.0047
Swin UNETR [51]	0.5171 ±0.0047	207.6704 ±2.4884	0.4921 ±0.0046	0.3438 ±0.0045	432.7990 ±2.8733	0.3300 ±0.0045	0.7037 ±0.0042	85.6554 ±1.7000	0.6805 ±0.0043	0.6599 ±0.0041	131.7022 ±1.9244	0.6201 ±0.0042	0.6137 ±0.0044	156.2208 ±2.2260	0.5824 ±0.0044
DA-TransUNet [52]	0.7783 ±0.0038	97.7011 ±1.4945	0.7563 ±0.0039	0.5907 ±0.0045	<b>166.4438</b> <b>±2.1574</b>	0.5610 ±0.0045	0.8319 ±0.0034	63.6652 ±1.4344	0.8143 ±0.0035	0.7948 ±0.0035	81.5234 ±1.6102	0.7594 ±0.0035	0.7780 ±0.0037	87.6505 ±1.6488	0.7489 ±0.0038
H2Former [10]	0.7490 ±0.0039	148.2938 ±2.0519	0.7220 ±0.0040	0.5627 ±0.0045	219.4662 ±2.3340	0.5323 ±0.0045	0.8095 ±0.0035	55.2702 ±1.0098	0.7859 ±0.0036	0.6369 ±0.0042	169.6482 ±2.0895	0.5934 ±0.0042	0.6815 ±0.0041	154.2361 ±2.0343	0.6460 ±0.0042
U-mamba [25]	0.6549 ±0.0043	132.5447 ±1.7257	0.6214 ±0.0043	0.3967 ±0.0045	315.6740 ±1.6164	0.3729 ±0.0045	0.7500 ±0.0040	75.1434 ±1.5002	0.7262 ±0.0040	0.5380 ±0.0043	192.8970 ±2.3236	0.4878 ±0.0043	0.5843 ±0.0044	181.0034 ±2.1725	0.5449 ±0.0043
DualSeg(ours)	<b>0.8251</b> <b>±0.0034</b>	<b>81.6201</b> <b>±1.5314</b>	<b>0.8022</b> <b>±0.0035</b>	0.5888 ±0.0045	235.8327 ±2.6482	0.5573 ±0.0045	<b>0.8848</b> <b>±0.0028</b>	<b>21.0608</b> <b>±0.2919</b>	<b>0.8630</b> <b>±0.0029</b>	<b>0.8393</b> <b>±0.0029</b>	57.6049 ±1.3786	<b>0.8123</b> <b>±0.0032</b>	<b>0.8195</b> <b>±0.0033</b>	<b>69.6369</b> <b>±1.5420</b>	<b>0.7938</b> <b>±0.0035</b>

specifically addresses the challenge of spatial heterogeneity by capturing long-range dependencies efficiently. The input feature map first undergoes downsampling to facilitate global context modeling at a reduced resolution.

**1) Z-Shift and Spatial Mixing:** To effectively model global interactions while preserving boundary integrity, we introduce a modified **Z-Shift** mechanism integrated with the Spatial Mixing block.

Crucially, unlike standard Vision Transformers that immediately flatten inputs, we apply the Z-Shift operator directly on the 2D feature maps before serialization. While the original Q-Shift in VRWKV discards pixels shifted beyond boundaries (zero-padding), our Z-Shift cyclically wraps these pixels to the opposite edge. This *zero-loss* shifting strategy ensures that spatial continuity is maintained, which is vital for delineating the complete contours of glomeruli.

After the spatial shift, the feature maps are flattened into token sequences and projected. The generation of the receptor, key, and value matrices is formulated as:

$$\mathbf{N}_s = \text{Linear}_N(\text{Flatten}(\text{Z-Shift}(\mathbf{X}))), \quad N \in \{R, K, V\}, \quad (3)$$

where  $\mathbf{X}$  denotes the input 2D feature map, and  $\text{Linear}_N$  represents the learnable projection weights. The flattened tokens then undergo the linear-complexity bidirectional attention aggregation:

$$\mathbf{S} = \sigma(\mathbf{R}_s) \odot \text{Bi-WKV}(\mathbf{K}_s, \mathbf{V}_s), \quad (4)$$

where  $\sigma(\cdot)$  is the sigmoid activation,  $\odot$  denotes element-wise multiplication, and Bi-WKV is the time-mixing operator that aggregates global context with linear complexity  $O(L)$ , efficiently capturing pairwise affinities between distant glomerular candidates.

**2) Channel Mixing:** Following spatial aggregation, the features undergo Channel Mixing to enable inter-channel communication. This module mirrors the gating mechanism of the spatial stage but focuses on feature refinement within the channel dimension. The transition is expressed as:

$$\mathbf{O}_c = \sigma(\mathbf{R}_c) \odot (\text{SqReLU}(\mathbf{K}_c) \cdot \mathbf{W}_v), \quad (5)$$

where  $\mathbf{R}_c$  and  $\mathbf{K}_c$  are derived from the spatially mixed features via linear projections, and SqReLU denotes the squared ReLU activation. The final output tokens are reshaped back into 2D spatial maps, fusing the global context captured by VRWKV with the local details from the previous Wave-Swin stage. This synergistic design ensures robust segmentation performance across variable glomerular morphologies.

### C. The Lightweight Decoder

To balance computational efficiency with segmentation precision, we adopt a lightweight decoding strategy. Following established practices [26], we selectively exclude the high-resolution features from the first CNN stage, as they contain excessive low-level noise that can degrade semantic consistency.

Consequently, we employ the *HamDecoder* [55] to fuse the feature maps from the subsequent three stages. As a pivotal component of our multi-scale interaction framework, this decoder utilizes Non-negative Matrix Factorization (NMF) to address the challenge of morphological prior integration. By modeling feature fusion as a matrix decomposition problem, the decoder effectively separates coherent semantic signals from background noise:

$$\mathbf{M} = \mathbf{D} \times \mathbf{C} + \mathbf{N}, \quad (6)$$

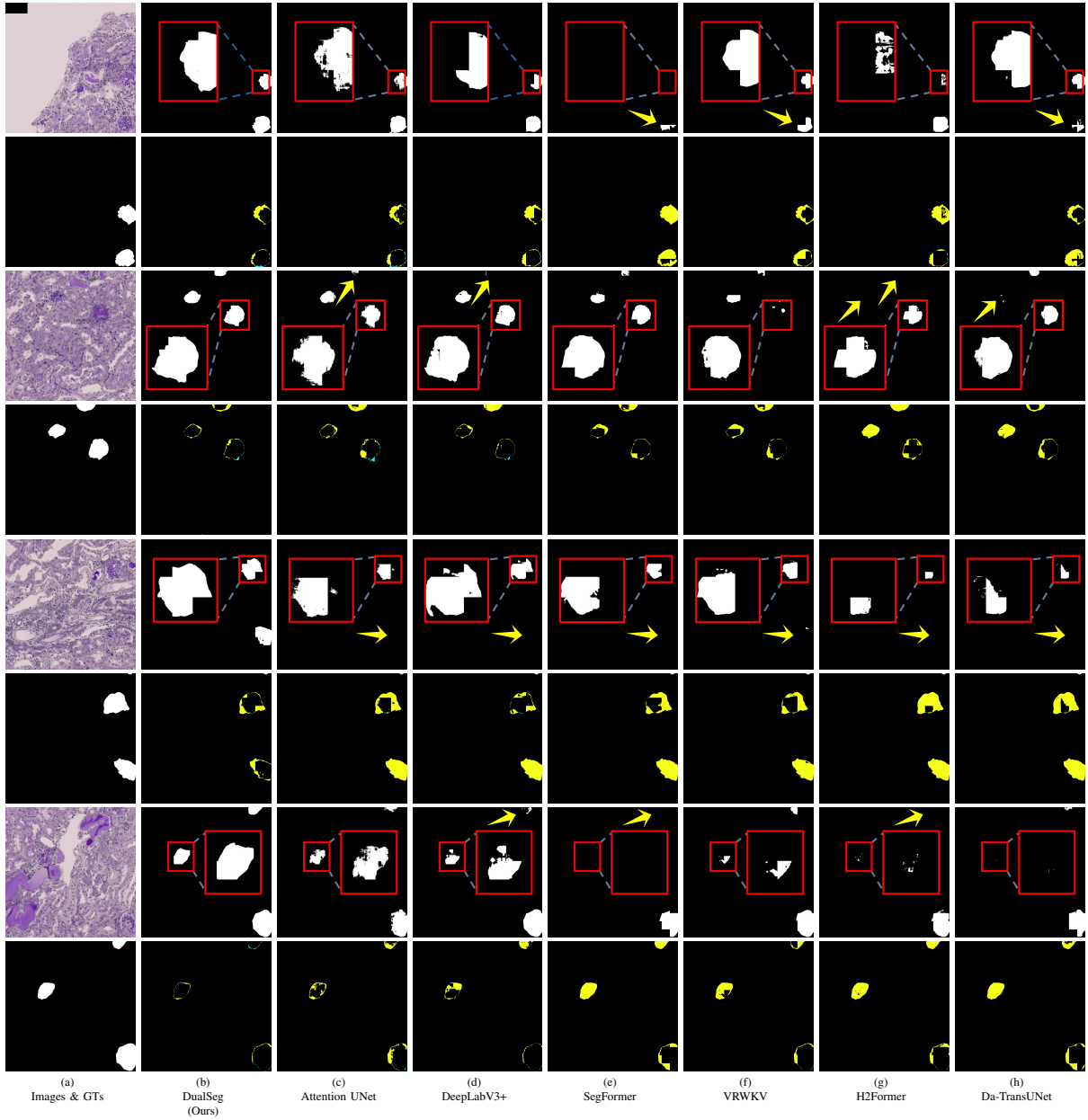


Fig. 6: Visual comparison on the KPIs test set. **Odd rows** display original images and inference masks; **even rows** show GT and error maps, where **yellow** and **green** denote under-segmentation and over-segmentation, respectively. Red boxes and matching arrows highlight magnified details and specific segmentation errors. **DualSeg** demonstrates superior performance in handling heterogeneous glomeruli with intricate boundaries.

where  $M$  denotes the aggregated feature mask, while  $D$ ,  $C$ , and  $N$  represent the learned *Dictionary*, *Codes*, and *Noise*, respectively. By reconstructing the mask using only the dictionary and codes ( $D \times C$ ), the model filters out the noise component  $N$ , yielding a refined and purer segmentation output.

This NMF-based decoding mechanism complements our Dual-Stage Hybrid encoder by explicitly enforcing low-rank constraints on the fused features, thereby enhancing boundary delineation without significant computational overhead.

## IV. EXPERIMENTS

In this section, we evaluate the proposed method on three glomerular segmentation datasets. We first introduce the benchmark datasets, implementation details, and evaluation metrics. Subsequently, we compare our method against SOTA approaches and perform ablation studies to validate the architectural design choices.

### A. Datasets

**Dataset I: Mice Glomeruli (KPIs).** The murine kidney dataset was sourced from the MICCAI 2024 Kidney Pathology

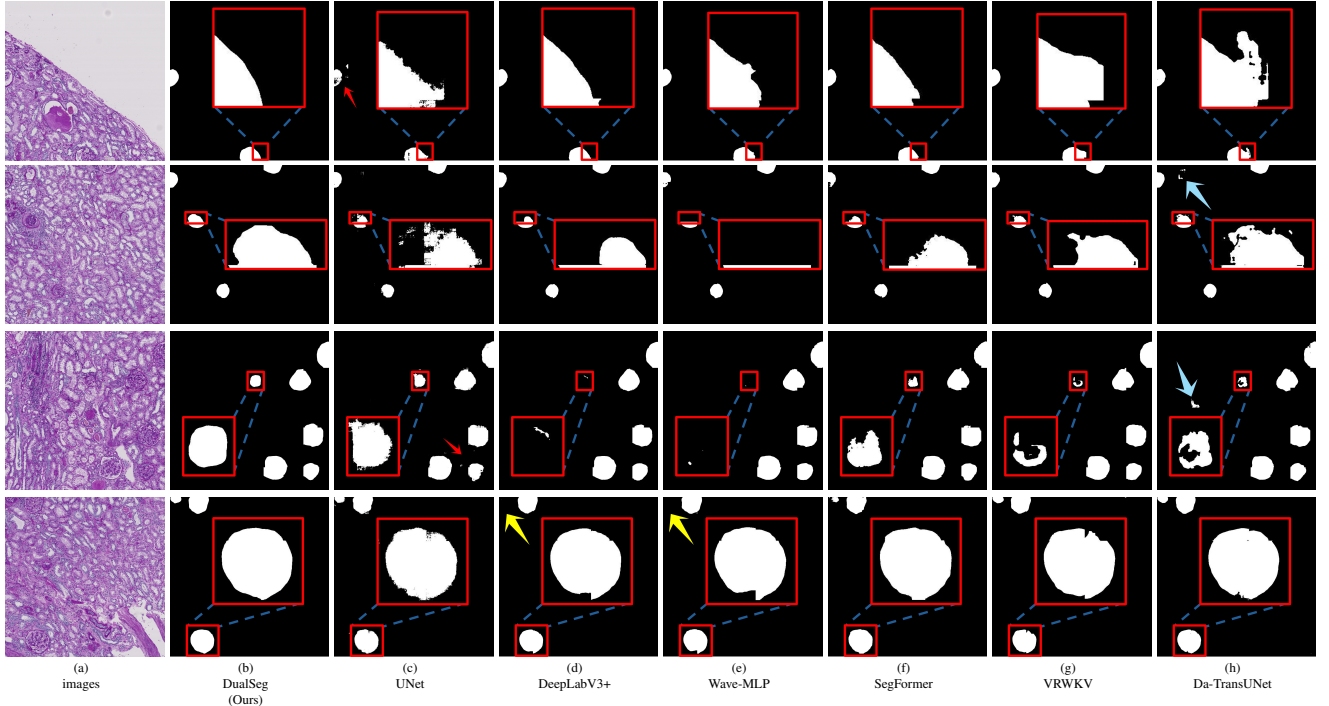


Fig. 7: Visual comparison on the HuBMAP test set. Since the official GT is private, we utilize the consensus of high-confidence predictions across multiple models as a reference. Local details are magnified to highlight segmentation challenges, with **yellow arrows** indicating suboptimal segmentation regions. **DualSeg** exhibits superior performance, evidenced by comprehensive edge processing and enhanced robustness against artifacts compared to baselines.

Image Segmentation (KPIs) challenge [56]. It includes PAS-stained images from four mouse models: normal, 5/6 nephrectomy (5/6Nx), diabetic nephropathy (DN), and NEP25 mice. To ensure consistency in patch-level evaluation, we utilized Task 1 data, provided as  $2,048 \times 2,048$  pixel patches containing functional tissue units (FTUs). The dataset comprises 5,213 training, 1,643 validation, and 2,305 test images. For model compatibility, we performed non-overlapping cropping to generate  $256 \times 256$  patches. We employed a 5-fold cross-validation strategy on the training/validation split (80%/20%), with final comparative results derived from the independent test set.

**Dataset II: Human Glomeruli (HuBMAP).** The first human dataset was obtained from the HuBMAP Kidney Challenge [57], focusing on FTU segmentation. It consists of 20 PAS-stained WSIs in TIFF format, averaging  $36,000 \times 29,000$  pixels. Glomeruli are annotated with precise polygonal contours. Following standard protocols [41], we partitioned the WSIs into 258,956 patches of size  $256 \times 256$  and implemented a 5-fold cross-validation (80% training, 20% validation). Final performance metrics were obtained by submitting inference results on the test set to the official Kaggle evaluation portal.

**Dataset III: Human Glomeruli (KPMP).** To assess cross-species generalization, we retrieved a second human dataset from the Kidney Precision Medicine Project (KPMP) Atlas Repository [58]. Four PAS-stained SVS format WSIs (avg. resolution  $84,000 \times 50,000$ ) were selected with corresponding masks. To rigorously validate generalization, models trained solely on the mouse KPIs dataset were directly applied to

this human dataset without retraining. For preprocessing consistency, KPMP WSIs were partitioned into  $2,048 \times 2,048$  patches.

### B. Baselines

We benchmark DualSeg against 14 representative methods spanning three architectural paradigms. *CNN-based models* include canonical baselines like **U-Net** [7] and **Attention U-Net** [49], the receptive-field-enhanced **DeepLabV3+** [42], and efficient modern architectures such as **SegNext** [26], **InceptionNext** [50], and **Wave-MLP** [22]. *Transformer-based models* encompass **SegFormer** [11] for hierarchical encoding, **VRWKV** [23] utilizing linear recurrent operators, and the SSM-integrated **VM-UNet-V2** [48]. Finally, *Hybrid models* feature U-shaped Transformer variants like **UNETR** [9] and **Swin UNETR** [51], alongside advanced fusion frameworks including **H2Former** [10], **DA-TransUNet** [52], and the Mamba-based **U-Mamba** [25].

### C. Evaluation Metrics

Performance is evaluated using the Dice Similarity Coefficient (DSC), Hausdorff Distance (95% percentile, HD95), and Intersection over Union (IoU). Let  $A$  and  $B$  denote the ground truth (GT) and predicted segmentation masks, respectively.

The **Dice coefficient** measures overlap:

$$\text{Dice} = \frac{2|A \cap B|}{|A| + |B|}. \quad (7)$$

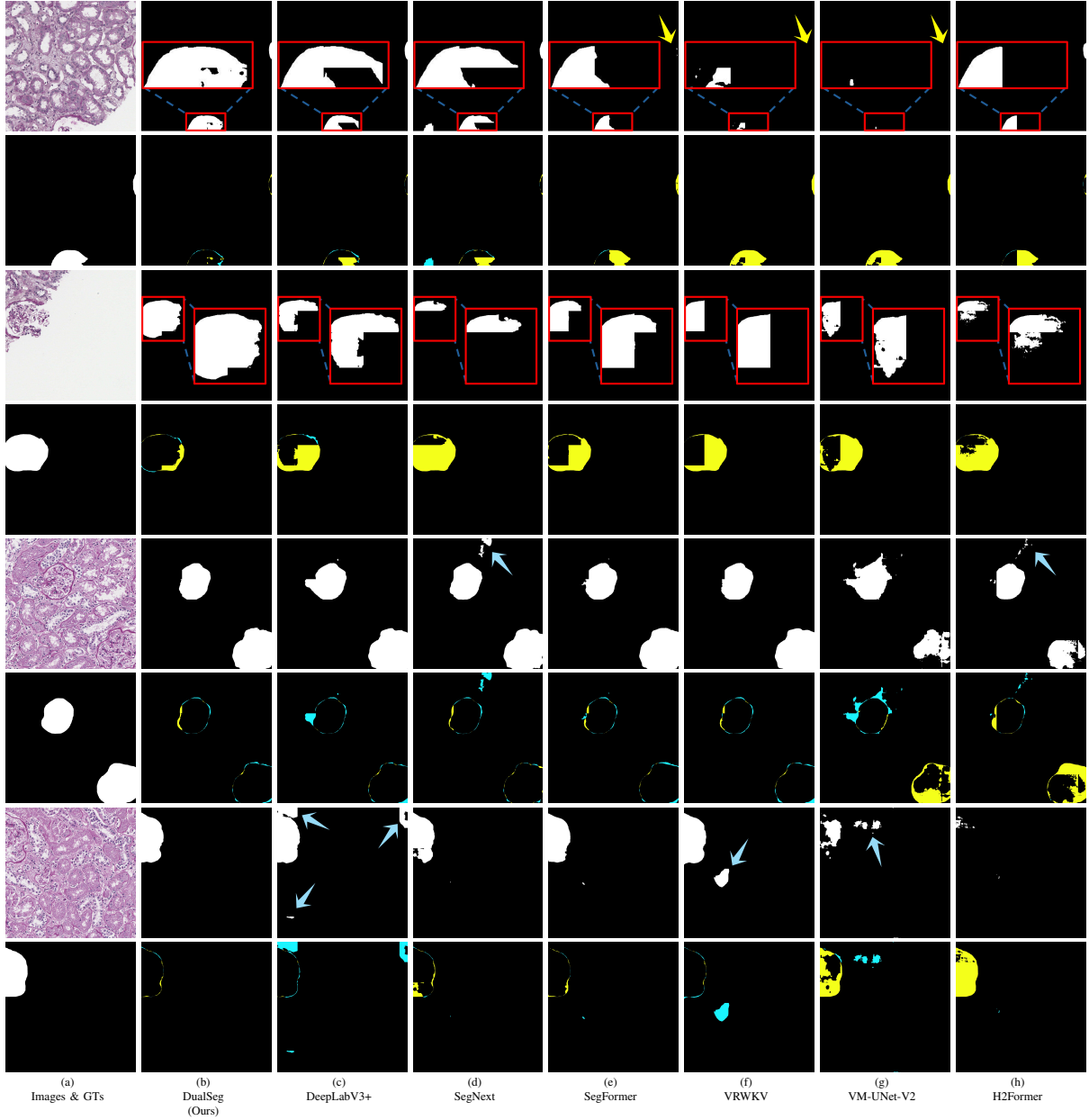


Fig. 8: Visual comparison on the held-out KPMP test set. **Odd rows** display original images and inference masks; **even rows** show GT and error maps, where **yellow** and **green** denote under-segmentation and over-segmentation, respectively. Red boxes and matching arrows highlight magnified details and segmentation errors. **DualSeg** exhibits unprecedented stability when handling cross-center and cross-species data.

The **HD95** quantifies boundary adherence by measuring the 95th percentile of the distances between surface points:

$$HD95 = \max_{p95} \left\{ \sup_{a \in A} \inf_{b \in B} d(a, b), \sup_{b \in B} \inf_{a \in A} d(b, a) \right\}, \quad (8)$$

where  $d(a, b)$  is the Euclidean distance between points  $a$  and  $b$ .

The **IoU** assesses the ratio of intersection to union:

$$IoU = \frac{|A \cap B|}{|A \cup B|}. \quad (9)$$

Note that for the HuBMAP dataset, we only have access to the Dice score, which is computed via the official evaluation

server.

#### D. Implementation Details

To mitigate overfitting, we applied data augmentation including horizontal/vertical flips and random rescaling. Models were trained for 20 epochs using the NAdam optimizer [59]. The learning rate was initialized at  $10^{-4}$  and adjusted via Cosine Annealing [60].

Training on both HuBMAP and KPIs datasets utilized  $256 \times 256$  patches with a batch size of 16. A critical adaptation was implemented for cross-dataset inference on KPMP: its patches were downsampled by a factor of 0.4. This scaling

TABLE IV: ABLATION STUDY OF MAJOR COMPONENTS ON THE TEST SET OF THE KPIs DATASET

Stage	Models	Layers			mDSC↑				
		Wave	Attention	VRWKV	DN	NEP25	Normal	5/6Nx	AVG
Sole-Stage	Wave [22]	✓	-	-	0.9165	0.9236	0.9322	0.8068	0.9036
	Attention [11]	-	✓	-	0.9223	0.9123	0.9249	0.8603	0.9099
	VRWKV [23]	-	-	✓	0.9209	0.9117	0.9268	0.8613	0.9108
Dual-Stage	Attention-Wave(Ours)	✓	✓	-	0.9192	0.9086	0.9241	0.8275	0.9019
	VRWKV-Wave(Ours)	✓	-	✓	0.8578	0.8168	0.8694	0.7011	0.8271
	Wave-Attention(Ours)	✓	✓	-	0.9267	0.9174	0.9334	0.8678	0.9171
	Wave-VRWKV(Ours)	✓	-	✓	0.9603	0.9349	0.9187	0.9007	0.9298

TABLE V: ABLATION STUDY OF THE PROPAGATION WINDOW ON THE TEST SET OF THE KPIs DATASET

Models	Propagation Window Size	mDSC↑				
		DN	NEP25	Normal	5/6Nx	AVG
Wave-MLP [22]	7	0.9299	0.9189	0.9361	0.8375	0.9131
	11	0.9228	0.9175	0.9366	0.8430	0.9075
	15	0.9227	0.9189	0.9144	0.8320	0.9012
	7-15	0.9365	0.9236	0.9322	0.8645	0.9146
DualSeg(Ours)	7	0.9544	0.9332	0.9245	0.8737	0.9205
	11	0.9571	0.9123	0.9224	0.8571	0.9132
	15	0.9450	0.9122	0.9111	0.8480	0.9112
	7-15	0.9603	0.9349	0.9187	0.9007	0.9298

TABLE VI: ABLATION STUDY OF THE SHIFT MODE ON THE TEST SET OF THE KPIs DATASET

Models	Shift Mode	mDSC↑				
		DN	NEP25	Normal	5/6Nx	AVG
VRWKV [23]	<i>Q-Shift</i>	0.9330	0.9232	0.9212	0.8738	0.9013
	<i>Z-Shift</i>	0.9344	0.9377	0.9255	0.8840	0.9108
DualSeg(Ours)	<i>Q-Shift</i>	0.9554	0.9220	0.9166	0.8902	0.9177
	<i>Z-Shift</i>	0.9603	0.9349	0.9187	0.9007	0.9298

strategy specifically addresses the inherent size discrepancy between murine and human glomeruli [41], enabling direct inference with KPIs-pretrained models without domain adaptation. Inference was performed using MONAI’s *Sliding Window Inference* [61] with a window size of  $256 \times 256$  to ensure resolution consistency. All experiments were conducted under identical settings to guarantee fair comparison.

## V. RESULTS

In this section, we evaluate the performance of DualSeg across three distinct renal pathology datasets, benchmarking it against established SOTA methods. Furthermore, we conduct ablation studies to validate the architectural design choices of the proposed dual-stage encoder and associated blocks. Comprehensive quantitative and qualitative analyses are presented below.

### A. Glomeruli Segmentation Results

1) *KPIs Dataset*: Table I quantifies the performance of DualSeg on the KPIs dataset, where it achieved the highest performance across all pathological categories with superior

stability, attaining an average mDSC of 92.98% and the lowest average HD95 of 66.85—outperforming top competing hybrid models like H2Former (90.52% mDSC) and DA-TransUNet (89.50% mDSC). In specific subgroup analyses, DualSeg robustly handled morphological extremes: in DN cases characterized by mild hypertrophy, it achieved an mDSC of 96.03%, surpassing the second-best VRWKV by 2.73% and reducing HD95 by 7.76 units; for NEP25 mice, it yielded an mDSC of 93.49%, significantly reducing the HD95 to 33.28 compared to SegNext’s 77.63; and most notably, in the challenging 5/6Nx subset characterized by severe fragmentation, DualSeg was the only method to exceed a 90% threshold (90.07% mDSC), surpassing VRWKV by 2.69% while achieving a substantially lower HD95 of 149.61 compared to 188.17.

2) *HuBMAP Dataset*: On the human HuBMAP dataset, DualSeg demonstrated dominant performance (Table II). The model achieved a Private mDSC of 89.79% and a Public mDSC of 83.73%. It outperformed the closest competitors, DA-TransUNet and SegFormer, by margins of 0.44% and 1.26% on the Private set, respectively. Crucially, DualSeg exhibited exceptional stability, with a standard deviation of only 0.0040 for the Private mDSC, contrasting sharply with the higher variance observed in baseline models.

3) *KPMP Dataset (Cross-Species Inference)*: To assess generalizability, we evaluated models pre-trained solely on the murine KPIs dataset directly on the human KPMP dataset without additional fine-tuning (Table III). DualSeg achieved a highly competitive average mDSC of 0.8195, surpassing SegFormer (0.8082) and significantly outperforming InceptionNext (0.5279). In terms of boundary delineation, DualSeg achieved an HD95 of 69.64, which is approximately one-third of the error recorded by VM-UNet-V2 (216.02). Furthermore, its IoU of 0.7938 surpassed other hybrid models by over 5%, validating the model’s capacity for robust cross-species and cross-center transfer learning.

### B. Ablation Studies

We performed systematic ablation experiments on the KPIs dataset to quantify the contributions of key architectural components: the dual-stage encoder, the dynamic propagation window in the Wave-Swin Block, and the Z-Shift operator in the VRWKV Block. Results are summarized in Tables IV, V, and VI.

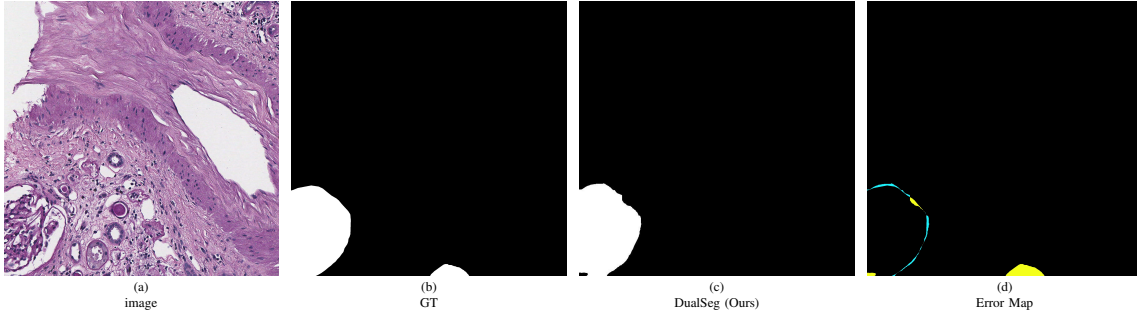


Fig. 9: A missegmentation case from the KPMP dataset. The yellow region at the bottom indicates that the model failed to segment the peripheral region of a globally sclerotic glomerulus.

**1) Effect of Dual-Stage Encoder:** Table IV contrasts single-stage architectures with the proposed dual-stage design. Single-stage variants employing only Wave-Swin Blocks, SegFormer-style self-attention, or VRWKV Blocks achieved average mDSCs of 90.36%, 90.99%, and 91.08%, respectively. The integrated Dual-Stage (Wave-VRWKV) architecture outperformed all single-stage counterparts with an average mDSC of 92.92%. We further investigated the impact of module sequencing. Reversing the feature extraction order (placing attention mechanisms before wave blocks) resulted in a significant performance decrease, lowering the average mDSC to 85.78% (Attention-Wave) and 91.63% (VRWKV-Wave). These findings corroborate the critical role of the proposed “local-to-global” refinement strategy.

**2) Effect of Dynamic Propagation Window:** Table V evaluates the impact of the dynamic Swin mechanism. The adaptive window strategy (range 7–15) achieved an average mDSC of 92.98%, outperforming all fixed-window configurations (sizes 7, 11, and 15). This advantage was most pronounced in the heterogeneous 5/6Nx subset, where the dynamic window improved mDSC by 2.70% compared to a fixed window size of 7.

**3) Effect of Z-Shift Operator:** Table VI demonstrates the efficacy of the Z-Shift operator over the conventional Q-Shift. Incorporating Z-Shift into DualSeg improved the average mDSC by 1.21%, with maximum gains observed in the NEP25 (1.29%) and 5/6Nx (1.05%) subsets. This confirms that the cyclic pixel wrapping strategy effectively mitigates information loss at patch boundaries.

### C. Visualization Results

To intuitively verify the superior performance of DualSeg in glomerular segmentation, we present qualitative comparisons on both the murine KPIs dataset and the human HuBMAP dataset in Fig. 6 and Fig. 7, respectively. These visualizations focus on challenging scenarios—including glomeruli with irregular shapes, ambiguous boundaries, and fragmented structures—which critically test the model’s ability to balance local texture discrimination with global context integration. Critical regions are magnified (marked with arrows) to highlight differences in segmentation precision.

For the mice KPIs dataset (Fig. 6), DualSeg accurately outlines renal glomeruli, avoiding the over-segmentation of

adjacent areas observed in other methods. While baselines such as SegFormer and DA-TransUNet exhibit difficulties in delineating glomerular regions under abnormal pathological conditions, DualSeg effectively captures lesions even in areas with subtle staining variations. Notably, DualSeg successfully reconstructs the structural continuity of damaged glomeruli, whereas Attention U-Net and H2Former fail to connect fragmented regions, resulting in disjointed masks.

In the human HuBMAP dataset (Fig. 7), DualSeg demonstrates superior robustness in handling large-scale, complex histopathological backgrounds. Human glomeruli exhibit significant size and spatial variability, often presenting ambiguity between sclerotic glomeruli and surrounding interstitial fibrosis. DualSeg clearly distinguishes these boundaries and preserves residual glomerular textures, whereas DeepLabV3+ and Wave-MLP frequently generate blurred boundaries with instances of missed detection. Furthermore, DualSeg outperforms DA-TransUNet and VRWKV, which tend to overemphasize main structures, resulting in either over-segmentation or incomplete segmentation.

Figure 8 illustrates the cross-species generalization on the human KPMP dataset using models pre-trained solely on mouse data. Baseline models display varying degrees of failure, manifesting as spurious outliers and misaligned segments that diverge from anatomical GT. Additionally, these baselines exhibit pronounced uncertainty, with noisy pseudo-segments in internal regions and discontinuous edge contours. Specifically, VM-UNet-V2 and H2Former show prominent under-detection artifacts, entirely omitting small or intricate glomerular regions. In stark contrast, DualSeg maintains sharp boundary delineation and internal consistency, demonstrating remarkable stability and confidence in cross-center, cross-species inference without domain adaptation.

## VI. DISCUSSION

Glomerular segmentation faces three fundamental challenges: **local texture discriminability**, **spatial heterogeneity**, and the **multi-scale mapping of morphological priors**. DualSeg directly targets these issues through a unified architecture. Its advantages over state-of-the-art (SOTA) methods are analyzed below.

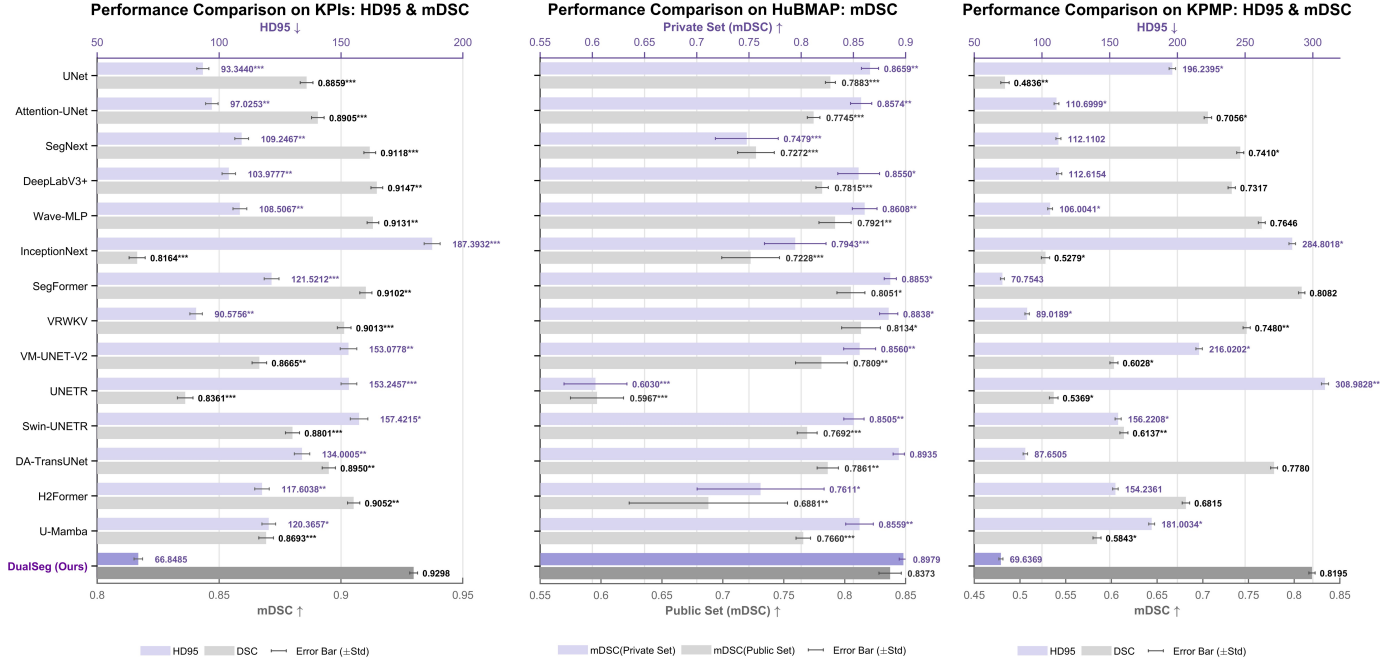


Fig. 10: Performance comparison between our DualSeg model and 14 baseline methods across three datasets. The comparison metrics include mDSC and HD95 for the KPIs and KPMP datasets (left and right panels, respectively), and mDSC for the HuBMAP dataset (middle panel). The error bars represent  $\pm$  standard deviation. Statistical significance levels are indicated by asterisks: \* $p < 0.05$ , \*\* $p < 0.01$ , \*\*\* $p < 0.001$ .

### A. Comparative Analysis with SOTA Methods

DualSeg effectively addresses the limitations of existing architectural paradigms through a unified framework. Unlike conventional CNNs (e.g., DeepLabV3+, InceptionNext) which are constrained by fixed receptive fields, DualSeg utilizes the Wave-Swin Block’s dynamic propagation window (Table V). This innovation enhances **local texture discriminability**, reducing HD95 by 26–37 on the KPIs dataset compared to CNN baselines and outperforming InceptionNext by 29.16% mDSC in cross-species tasks.

Furthermore, while Transformers typically excel at global context but compromise local detail due to patch flattening, DualSeg integrates a Z-Shift operator within the VRWKV block to preserve edge integrity. This design mitigates the information loss inherent in standard Q-Shift operations (Table VI) and models **spatial heterogeneity** more effectively, allowing DualSeg to exceed VM-UNet-V2 by 21.67% on the external KPMP dataset.

Finally, in contrast to existing hybrids (e.g., H2Former, DA-TransUNet) that suffer from a “semantic gap” or the high computational costs of U-Mamba (Fig. 1), DualSeg employs a sequential *local-to-global* refinement strategy. This structured integration ensures precise **morphological prior mapping**, enabling the model to outperform H2Former by 13.68% on HuBMAP and surpass U-Mamba by 23.52% on KPMP. By dynamically adapting to morphological variability and seamlessly integrating features, DualSeg establishes a robust and efficient backbone for renal histology analysis.

### B. Failure Case Analysis

Fig. 9 reveals that the model occasionally fails to detect globally sclerotic glomeruli in the KPMP dataset. This limitation stems primarily from two factors: the partial truncation of peripheral glomeruli during WSI tiling, which compromises morphological context, and the significant divergence of unseen, extreme pathological variants. To mitigate this, future work could increase patch sizes to preserve boundary information or, more efficiently, integrate uncertainty-guided semi-supervised learning. This strategy aims to enhance robustness against rare phenotypes without incurring excessive computational overhead.

### C. Clinical Relevance

DualSeg exhibits statistically significant superiority ( $p < 0.05$ – $0.001$ ; Fig. 10) and exceptional reproducibility, evidenced by a minimal standard deviation (0.004) on the HuBMAP dataset. Its ability to accurately resolve diverse morphologies—ranging from mild hypertrophy to severe fragmentation—enables the precise quantification of pathological biomarkers like sclerosis and fibrosis. Furthermore, the model’s robust performance on the cross-species KPMP dataset supports standardized CKD monitoring. By mitigating inter-observer variability and reducing manual annotation burdens, DualSeg provides a scalable solution for multi-center clinical trials and routine diagnostic workflows.

### D. Limitations

While DualSeg achieves superior performance in glomerular segmentation, several limitations remain to be addressed.

First, although the VRWKV Block utilizes linear complexity attention, it introduces non-negligible inference overhead when processing ultra-high-resolution WSIs with gigapixel dimensions, which may restrict its real-time applicability in clinical workflows. Second, while DualSeg exhibits robustness across murine and human datasets, its generalization to rare pathological subtypes (e.g., focal segmental and global glomerulosclerosis with atypical morphological patterns) remains underexplored, as these cases were underrepresented in the evaluated datasets.

## VII. CONCLUSION

We present DualSeg, a unified hybrid framework designed to resolve the conflicting demands of local texture discriminability, spatial heterogeneity, and multi-scale morphological mapping in renal histopathology. By synergizing a Wave-Swin encoder featuring dynamic propagation windows with a VRWKV module employing Z-Shift operators, the model effectively balances fine-grained feature extraction with efficient global context modeling. Extensive evaluations across murine (KPIs) and human (HuBMAP, KPMP) datasets demonstrate that DualSeg outperforms state-of-the-art methods, delivering superior mDSC and lowest HD95 scores while exhibiting robust cross-species generalization. Ablation studies further validate the critical role of the dual-stage architecture in mitigating boundary loss and adapting to morphological variations. These findings establish DualSeg as a precise, scalable backbone for automated glomerular segmentation, with broad potential for complex histopathological analysis.

- [1] S. L. James, “A systematic analysis for the global burden of disease study 2017,” *The Lancet*, vol. 392, no. 10159, pp. 1789–1858, 2018.
- [2] T. K. Chen, D. H. Knicely, and M. E. Grams, “Chronic kidney disease diagnosis and management: a review,” *Jama*, vol. 322, no. 13, pp. 1294–1304, 2019.
- [3] C. Zoccali, R. Vanholder, Z. A. Massy, A. Ortiz, P. Sarafidis, F. W. Dekker, D. Fliser, D. Fouque, G. H. Heine, and K. J. Jager, “The systemic nature of ckd,” *Nat. Rev. Nephrol.*, vol. 13, no. 6, pp. 344–358, 2017.
- [4] J. M. Muñoz-Felix, B. Oujo, and J. M. Lopez-Novoa, “The role of endoglin in kidney fibrosis,” *Expert Rev. Mol. Med.*, vol. 16, p. e18, 2014.
- [5] A. Z. Rosenberg and J. B. Kopp, “Focal segmental glomerulosclerosis,” *Clin. J. Am. Soc. Nephrol.*, vol. 12, no. 3, pp. 502–517, 2017.
- [6] M. Aljabri, M. AlAmir, M. AlGhamdi, M. Abdel-Mottaleb, and F. Collado-Mesa, “Towards a better understanding of annotation tools for medical imaging: a survey,” *Multimed. Tools Appl.*, vol. 81, no. 18, pp. 25 877–25 911, 2022.
- [7] O. Ronneberger, P. Fischer, and T. Brox, “U-net: Convolutional networks for biomedical image segmentation,” in *Medical Image Computing and Computer-Assisted Intervention – MICCAI 2015*, N. Navab, J. Hornegger, W. M. Wells, and A. F. Frangi, Eds. Cham: Springer International Publishing, 2015, pp. 234–241.
- [8] J. Chen, Y. Lu, Q. Yu, X. Luo, E. Adeli, Y. Wang, L. Lu, A. L. Yuille, and Y. Zhou, “Transunet: Transformers make strong encoders for medical image segmentation,” *arXiv preprint arXiv:2102.04306*, 2021.
- [9] A. Hatamizadeh, Y. Tang, V. Nath, D. Yang, A. Myronenko, B. Landman, H. R. Roth, and D. Xu, “Unetr: Transformers for 3d medical image segmentation,” in *Proceedings of the IEEE/CVF winter conference on applications of computer vision*, 2022, pp. 574–584.
- [10] A. He, K. Wang, T. Li, C. Du, S. Xia, and H. Fu, “H2former: An efficient hierarchical hybrid transformer for medical image segmentation,” *IEEE Trans. Med. Imaging*, vol. 42, no. 9, pp. 2763–2775, 2023.
- [11] E. Xie, W. Wang, Z. Yu, A. Anandkumar, J. M. Alvarez, and P. Luo, “Segformer: Simple and efficient design for semantic segmentation with transformers,” *Adv. neural inf. proces. syst.*, vol. 34, pp. 12 077–12 090, 2021.
- [12] F. Allender, R. Allégre, C. Wemmert, and J.-M. Dischler, “Conditional image synthesis for improved segmentation of glomeruli in renal histopathological images,” in *2022 IEEE-EMBS International Conference on Biomedical and Health Informatics (BHI)*, 2022, pp. 1–5.
- [13] Y. Liu, “A hybrid cnn-transxnet approach for advanced glomerular segmentation in renal histology imaging,” *Int. J. Comput. Int. Sys.*, vol. 17, no. 1, p. 126, 2024.
- [14] B. Shickel, N. Lucarelli, A. S. Rao, D. Yun, K. C. Moon, S. S. Han, and P. Sarder, “Spatially aware transformer networks for contextual prediction of diabetic nephropathy progression from whole slide images,” *medRxiv*, 2023.
- [15] G. M. Dimitri, P. Andreini, S. Bonechi, M. Bianchini, A. Mecocci, F. Scarselli, A. Zacchi, G. Garosi, T. Marcuzzo, and S. A. Tripodi, “Deep learning approaches for the segmentation of glomeruli in kidney histopathological images,” *Mathematics*, vol. 10, no. 11, 2022. [Online]. Available: <https://www.mdpi.com/2227-7390/10/11/1934>
- [16] B. Ginley, K.-Y. Jen, A. Rosenberg, F. Yen, S. Jain, A. Fogo, and P. Sarder, “Neural network segmentation of interstitial fibrosis, tubular atrophy, and glomerulosclerosis in renal biopsies,” *arXiv preprint arXiv:2002.12868*, 2020.
- [17] K. M. Hosny, T. Magdy, N. A. Lashin, K. Apostolidis, and G. A. Papakostas, “Refined color texture classification using cnn and local binary pattern,” *Mathematical Problems in Engineering*, vol. 2021, no. 1, p. 5567489, 2021.
- [18] G. Kaur, M. Garg, S. Gupta, S. Juneja, J. Rashid, D. Gupta, A. Shah, and A. Shaikh, “Automatic identification of glomerular in whole-slide images using a modified unet model,” *Diagnostics*, vol. 13, no. 19, p. 3152, 2023.
- [19] H. Sun, J. Xu, and Y. Duan, “Paratranscnn: Parallelized transcnn encoder for medical image segmentation,” *arXiv preprint arXiv:2401.15307*, 2024.
- [20] J. Zhang, J. D. Lu, B. Chen, S. Pan, L. Jin, Y. Zheng, and M. Pan, “Vision transformer introduces a new vitality to the classification of renal pathology,” *BMC nephrology*, vol. 25, no. 1, p. 337, 2024.
- [21] G. V. Bharadwaj, Y. R. Sree, J. L. Varshita, and S. Chebrolu, “Ensemble model of u-net efficientnet-b3, u-net efficientnet b6, coat, segformer for segmenting functional tissue units in various human organs,” in *2023 14th International Conference on Computing Communication and Networking Technologies (ICCCNT)*. IEEE, 2023, pp. 1–8.
- [22] Y. Tang, K. Han, J. Guo, C. Xu, Y. Li, C. Xu, and Y. Wang, “An image patch is a wave: Phase-aware vision mlp,” in *Proceedings of the IEEE/CVF conference on computer vision and pattern recognition*, 2022, pp. 10 935–10 944.
- [23] Y. Duan, W. Wang, Z. Chen, X. Zhu, L. Lu, T. Lu, Y. Qiao, H. Li, J. Dai, and W. Wang, “Vision-rwkv: Efficient and scalable visual perception with rwkv-like architectures,” *arXiv preprint arXiv:2403.02308*, 2024.
- [24] J. Ruan, J. Li, and S. Xiang, “Vm-unet: Vision mamba unet for medical image segmentation,” *ACM Transactions on Multimedia Computing, Communications and Applications*, 2024.
- [25] J. Ma, F. Li, and B. Wang, “U-mamba: Enhancing long-range dependency for biomedical image segmentation,” *arXiv preprint arXiv:2401.04722*, 2024.
- [26] M.-H. Guo, C.-Z. Lu, Q. Hou, Z. Liu, M.-M. Cheng, and S.-M. Hu, “Segnext: Rethinking convolutional attention design for semantic segmentation,” *Adv. neural inf. proces. syst.*, vol. 35, pp. 1140–1156, 2022.
- [27] A. Fourcade and R. H. Khonsari, “Deep learning in medical image analysis: A third eye for doctors,” *Journal of stomatology, oral and maxillofacial surgery*, vol. 120, no. 4, pp. 279–288, 2019.
- [28] Q. Pu, Z. Xi, S. Yin, Z. Zhao, and L. Zhao, “Advantages of transformer and its application for medical image segmentation: a survey,” *BioMedical engineering online*, vol. 23, no. 1, p. 14, 2024.
- [29] F. Renard, S. Guedria, N. D. Palma, and N. Vuillerme, “Variability and reproducibility in deep learning for medical image segmentation,” *Scientific Reports*, vol. 10, no. 1, p. 13724, 2020.
- [30] G. E. Lees, R. E. Cianciolo, and F. J. Clubb Jr, “Renal biopsy and pathologic evaluation of glomerular disease,” *Topics in companion animal medicine*, vol. 26, no. 3, pp. 143–153, 2011.
- [31] T. Kato, R. Relator, H. Ngouv, Y. Hirohashi, O. Takaki, T. Kakimoto, and K. Okada, “Segmental hog: new descriptor for glomerulus detection in kidney microscopy image,” *Bmc Bioinformatics*, vol. 16, pp. 1–16, 2015.

- [32] P. Sarder, B. Ginley, and J. E. Tomaszewski, "Automated renal histopathology: digital extraction and quantification of renal pathology," in *Medical Imaging 2016: Digital Pathology*, vol. 9791. SPIE, 2016, pp. 112–123.
- [33] D. Govind, B. Ginley, B. Lutnick, J. E. Tomaszewski, and P. Sarder, "Glomerular detection and segmentation from multimodal microscopy images using a butterworth band-pass filter," in *Medical Imaging 2018: Digital Pathology*, vol. 10581. SPIE, 2018, pp. 297–303.
- [34] S. Sheehan, S. Mawe, R. E. Cianciolo, R. Korstanje, and J. M. Mahoney, "Detection and classification of novel renal histologic phenotypes using deep neural networks," *The American Journal of Pathology*, vol. 189, no. 9, pp. 1786–1796, 2019.
- [35] Y. Kawazoe, K. Shimamoto, R. Yamaguchi, Y. Shintani-Domoto, H. Uozaki, M. Fukayama, and K. Ohe, "Faster r-cnn-based glomerular detection in multistained human whole slide images," *J. Imaging*, vol. 4, no. 7, p. 91, 2018.
- [36] X. Han, G. Zhang, and X. Wang, "Glomerular microscopic image segmentation based on convolutional neural network," in *2019 Chinese Control Conference (CCC)*. IEEE, 2019, pp. 8343–8348.
- [37] N. Altini, G. D. Cascarano, A. Brunetti, I. De Feudis, D. Buongiorno, M. Rossini, F. Pesce, L. Gesualdo, and V. Bevilacqua, "A deep learning instance segmentation approach for global glomerulosclerosis assessment in donor kidney biopsies," *Electronics*, vol. 9, no. 11, p. 1768, 2020.
- [38] G. D. Cascarano, F. S. Debitonto, R. Lemma, A. Brunetti, D. Buongiorno, I. De Feudis, A. Guerriero, M. Rossini, F. Pesce, L. Gesualdo *et al.*, "An innovative neural network framework for glomerulus classification based on morphological and texture features evaluated in histological images of kidney biopsy," in *Intelligent Computing Methodologies: 15th International Conference, ICIC 2019, Nanchang, China, August 3–6, 2019, Proceedings, Part III 15*. Springer, 2019, pp. 727–738.
- [39] J. N. Marsh, M. K. Matlock, S. Kudose, T.-C. Liu, T. S. Stappenbeck, J. P. Gaut, and S. J. Swamidas, "Deep learning global glomerulosclerosis in transplant kidney frozen sections," *IEEE Trans. Med. Imaging*, vol. 37, no. 12, pp. 2718–2728, 2018.
- [40] G. Bueno, M. M. Fernandez-Carrobles, L. Gonzalez-Lopez, and O. Deniz, "Glomerulosclerosis identification in whole slide images using semantic segmentation," *Comput. Meth. Programs Biomed.*, vol. 184, p. 105273, 2020.
- [41] P. Andreini, S. Bonechi, and G. M. Dimitri, "Enhancing glomeruli segmentation through cross-species pre-training," *Neurocomputing*, vol. 563, p. 126947, 2024.
- [42] B. Ginley, K.-Y. Jen, A. Rosenberg, F. Yen, S. Jain, A. Fogo, and P. Sarder, "Neural network segmentation of interstitial fibrosis, tubular atrophy, and glomerulosclerosis in renal biopsies," *arXiv preprint arXiv:2002.12868*, 2020.
- [43] J. M. J. Valanarasu and V. M. Patel, "Unext: Mlp-based rapid medical image segmentation network," in *International conference on medical image computing and computer-assisted intervention*. Springer, 2022, pp. 23–33.
- [44] F. N. Saikia, Y. Iwahori, T. Suzuki, M. K. Bhuyan, A. Wang, and B. Kijisirikul, "Mlp-unet: glomerulus segmentation," *IEEE Access*, vol. 11, pp. 53 034–53 047, 2023.
- [45] I. O. Tolstikhin, N. Houlsby, A. Kolesnikov, L. Beyer, X. Zhai, T. Unterthiner, J. Yung, A. Steiner, D. Keysers, J. Uszkoreit *et al.*, "Mlp-mixer: An all-mlp architecture for vision," *Adv. neural inf. proces. syst.*, vol. 34, pp. 24 261–24 272, 2021.
- [46] F. Yang, Q. He, Y. Wang, S. Zeng, Y. Xu, J. Ye, Y. He, T. Guan, Z. Wang, and J. Li, "Unsupervised stain augmentation enhanced glomerular instance segmentation on pathology images," *International Journal of Computer Assisted Radiology and Surgery*, vol. 20, no. 2, pp. 225–236, 2025.
- [47] Q. He, S. Zeng, S. Ge, Y. Wang, J. Ye, Y. He, T. Guan, Z. Wang, and J. Li, "Identifying and matching 12-level multistained glomeruli via deep learning for diagnosis of glomerular diseases," *International Journal of Imaging Systems and Technology*, vol. 34, no. 2, p. e23032, 2024.
- [48] M. Zhang, Y. Yu, S. Jin, L. Gu, T. Ling, and X. Tao, "Vm-unet-v2: rethinking vision mamba unet for medical image segmentation," in *International symposium on bioinformatics research and applications*. Springer, 2024, pp. 335–346.
- [49] O. Oktay, J. Schlemper, L. L. Folgoc, M. Lee, M. Heinrich, K. Misawa, K. Mori, S. McDonagh, N. Y. Hammerla, B. Kainz *et al.*, "Attention u-net: Learning where to look for the pancreas," *arXiv preprint arXiv:1804.03999*, 2018.
- [50] W. Yu, P. Zhou, S. Yan, and X. Wang, "Inceptionnext: When inception meets convnext," in *Proceedings of the IEEE/cvf conference on computer vision and pattern recognition*, 2024, pp. 5672–5683.
- [51] A. Hatamizadeh, V. Nath, Y. Tang, D. Yang, H. R. Roth, and D. Xu, "Swin unetr: Swin transformers for semantic segmentation of brain tumors in mri images," in *International MICCAI brainlesion workshop*. Springer, 2021, pp. 272–284.
- [52] G. Sun, Y. Pan, W. Kong, Z. Xu, J. Ma, T. Racharak, L.-M. Nguyen, and J. Xin, "Da-transunet: integrating spatial and channel dual attention with transformer u-net for medical image segmentation," *Front. Bioeng. Biotechnol.*, vol. 12, p. 1398237, 2024.
- [53] Y. Gu, R. Ruan, Y. Yan, J. Zhao, W. Sheng, L. Liang, and B. Huang, "Glomerulus semantic segmentation using ensemble of deep learning models," *Arab. J. Sci. Eng.*, vol. 47, no. 11, pp. 14 013–14 024, 2022.
- [54] M. Hermsen, T. de Bel, M. Den Boer, E. J. Steenberg, J. Kers, S. Florquin, J. J. Roelofs, M. D. Stegall, M. P. Alexander, B. H. Smith *et al.*, "Deep learning-based histopathologic assessment of kidney tissue," *J. Am. Soc. Nephrol.*, vol. 30, no. 10, pp. 1968–1979, 2019.
- [55] Z. Geng, M.-H. Guo, H. Chen, X. Li, K. Wei, and Z. Lin, "Is attention better than matrix decomposition?" *arXiv preprint arXiv:2109.04553*, 2021.
- [56] Y. Tang, Y. He, V. Nath, P. Guo, R. Deng, T. Yao, Q. Liu, C. Cui, M. Yin, Z. Xu *et al.*, "Holohisto: end-to-end gigapixel wsi segmentation with 4k resolution sequential tokenization," *arXiv preprint arXiv:2407.03307*, 2024.
- [57] H. Addison, L. Andy, S. Bud, T. Eddie, K. Jarek, B. Katy, G. Leah, N. Marcos, C. Phil, H. Richard, W. Rick, and J. Yingnan. (2021) Hubmap - hacking the kidney. [Online]. Available: <https://kaggle.com/competitions/hubmap-kidney-segmentation>
- [58] KPMP Consortium. (2021) Kidney precision medicine project. National Institute of Diabetes and Digestive and Kidney Diseases (NIDDK). Accessed: 2025-12-11. [Online]. Available: <https://atlas.kpmp.org/repository>
- [59] T. Dozat, "Incorporating nesterov momentum into adam," in *Proceedings of 4th International Conference on Learning Representations (ICLR)*, 2016, pp. 1–4.
- [60] I. Loshchilov and F. Hutter, "Sgdr: Stochastic gradient descent with warm restarts," *arXiv preprint arXiv:1608.03983*, 2016.
- [61] M. J. Cardoso, W. Li, R. Brown, N. Ma, E. Kerfoot, Y. Wang, B. Murray, A. Myronenko, C. Zhao, D. Yang *et al.*, "Monai: An open-source framework for deep learning in healthcare," *arXiv preprint arXiv:2211.02701*, 2022.